Journal of the Brazilian Society of Mechanical Sciences and Engineering (2020) 42:419
https://doi.org/10.1007/s40430-020-02498-w

TECHNICAL PAPER

Numerical and experimental analysis of fretting fatigue performance of the 1350-H19 aluminum alloy

Rodrigo L. Pereira[1,2] · José I. M. Díaz[1] · Jorge L. A. Ferreira[1] · Cosme R. M. da Silva[1] · José A. Araújo[1]

Received: 17 February 2020 / Accepted: 7 July 2020 / Published online: 18 July 2020

Abstract
When power transmission cables are subjected to oscillatory displacements, due to the wind vibration, fretting fatigue phenomenon takes place, being the main prompter of catastrophic failure. In this work, we investigate the behavior of an 1350-H19 aluminum wire, that is a structural element of the IBIS (ACSR 397.5 MCM) conductor cable, when subjected to fretting fatigue. For this, a numerical methodology was developed, in which a three-dimensional finite element model was constructed to obtain the maximum Von Mises stresses in the vicinity of the wire-to-wire contact. Thus, a stress-based uniaxial fatigue approach was implemented, resulting in S–N curves. The effect of mean stresses on fatigue behavior was also considered through a series of well-known models. The data generated in this process were validated with experimentally obtained S–N curves on a MTS 322.21 machine, especially modified for this purpose. Most of the results were within the limits considered, with slightly conservative tendencies. A new value of adjustable material parameter has been proposed to be used with Walker's model, increasing the accuracy of the predictions.

Keywords Fatigue · Fretting · ACSR conductor · Transmission line · Finite element simulation

1 Introduction

When a joint of mechanical components is subjected to oscillating forces, relative tangential displacements can occur resulting in surface damage, such as fretting wear[1]. In addition, due to large stress gradients, cracks may also appear and its propagation may result in catastrophic failure by fretting fatigue[2]. Particularly, this phenomenon has been encountered on both steel cables and power transmission lines. Frequently, these cables operates in regions of strong winds, causing a nonstop structural movement. This so-called wind vibration is the main cause of small amplitude displacements at the contact areas between wires. Adding the fact that those structures have to carry their own weight, since they are frequently suspended, micro-cracks may grow causing fretting fatigue problems[3, 4].

Such observations, and the fact that these kinds of structures often execute a key role in many engineering applications, led various researchers to investigate ways of solving those issues. Among the various contributors, Knapp and Chiu[5] played an important role in the study of uniaxial fatigue in electrical conductor cables, developing a theoretical model, supported by experimental analyses. However, the authors chose to neglect the fretting fatigue between the inner wires, so that the model could only be used in cases where the relative displacement of these structures could also be neglected. Shortly thereafter, Hobbs and Raoof[6, 7] proposed a stress-based model to predict the life of wire ropes subjected to uniaxial fatigue. In their work, the

Technical Editor: João Marciano Laredo dos Reis.

✉ Rodrigo L. Pereira
pereira@fem.unicamp.br

José I. M. Díaz
jimonroyd@gmail.com

Jorge L. A. Ferreira
jorge@unb.br

Cosme R. M. da Silva
cosmeroberto@unb.br

José A. Araújo
alex07@unb.br

[1] Department of Mechanical Engineering, Faculty of Technology, University of Brasília, Brasília 70910-900, Brazil

[2] Present Address: Department of Computational Mechanics, School of Mechanical Engineering, University of Campinas, Rua Mendeleyev 200, Campinas 13083-860, Brazil

Table 1 General properties of the Al 1350-H19

S_y (MPa)	S_{ut} (MPa)	E (MPa)	S'_e (MPa)	S_{fB} (MPa)
165	186	68900	48.3	198.73

researchers applied the equations obtained by Thomas and Hoersch[8], as summarized by Knapp and Chiu[5], in order to find the maximum Von Mises stresses below the cable surface, when subjected to axial loads, but in this time considering the partial slip between the inner layers of wires. More recently, Wokem et al.[9, 10] proposed the use of the finite element method (FEM) to numerically model entire steel cables and wire ropes, obtaining the maximum stresses below the surface of these structures. Then, a stress-based uniaxial fatigue approach was implemented to predict the life.

In this context, and aiming at a better understanding of the conditions that cause fretting in the internal components of the IBIS (ACSR 397.5 MCM) power transmission cable, the present work studies, in a numerical and experimental manner, the fatigue life of a 1350-H19 aluminum wire, when subjected to contact with another wire of identical constitution. On an experimental perspective, the analysis were conducted using a modified MTS 322.21 machine which, after simulating the operational conditions of the wires in an IBIS cable, generated data that culminated on its S–N curves. Then, the numerical analysis was made use of the finite element method to obtain the maximum Von Mises stresses at the vicinity of the contact that, subsequently, was used on the fatigue analysis of the wire. Several well-known models were considered in this process to account for the mean stress effects. Finally, to validate the numerical methodology, these results were compared with the experimental data collected.

2 Materials and methods

2.1 Experimental material and test machine

The material of which the tested specimens were made was the 1350-H19 aluminum alloy, whose general properties are summarized in Table 1. Here, S_y is the yield tensile strength, S_{ut} is the ultimate tensile strength, E is the modulus of elasticity, S'_e is the endurance limit and S_{fB} is the true fracture strength.

The specimens were taken from a sample of ACSR IBIS overhead conductor which had a nominal diameter of 19.88 mm and consisted of two layers of 1350-H19 aluminum wires, with a diameter of 3.139 mm each, being organized in a 16 outer and 10 inner wires composition. These were wrapped in a core formed by seven steel wires of 2.441 mm in diameter. In order to avoid torsional stresses when the overhead conductor is subjected to tensile forces, it is common that the layers are mounted in a helix. Figure 1 shows schematically the cross section of an ACSR conductor, with the, respectively, helix angles indicated by layer.

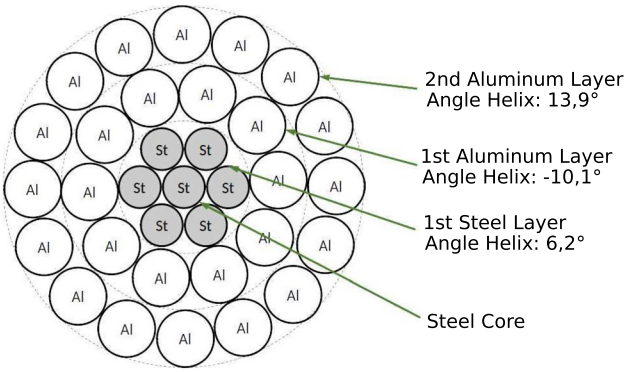

Fig. 1 Schematic cross-sectional view of an Ibis ACSR conductor illustrating its layers and respective helix angles

The apparatus developed to experimentally simulate the fretting fatigue conditions that occur in the ACSR conductor is inspired by the one used by Hills and Nowell[1] and is schematically shown in Fig. 2, with detailed viewing of the contact area referred as A. In order to create the cyclic load over the specimen, a MTS 322.21 hydraulic servo machine (1) was modified. Here, the tangential loads and relative displacements were transmitted by the actuator (2) to the pad (13) by the rigid frame (4). The recordings were made by the loading cell (3). To apply a cyclic bulk load over the specimen (12), the hydraulic actuator (9) was used. The loading cells (5) and (8) kept these records. The normal contact forces were applied by the actuator (10) over the pad, which had the records kept in loading cell (11). The clamping jaws (6) and (7) were used to hold the specimen.

2.2 Experimental methodology

In order to properly describe the experimental procedures adopted it is important to define the stress ratio, R, as well as the alternating, S_a, and mean, S_m, stresses, which are all functions of the maximum, S_{max}, and minimum, S_{min}, stresses, as shown in Eqs. 1, 2 and 3:

$$R = \frac{S_{min}}{S_{max}}, \tag{1}$$

$$S_a = \frac{S_{max} - S_{min}}{2}, \tag{2}$$

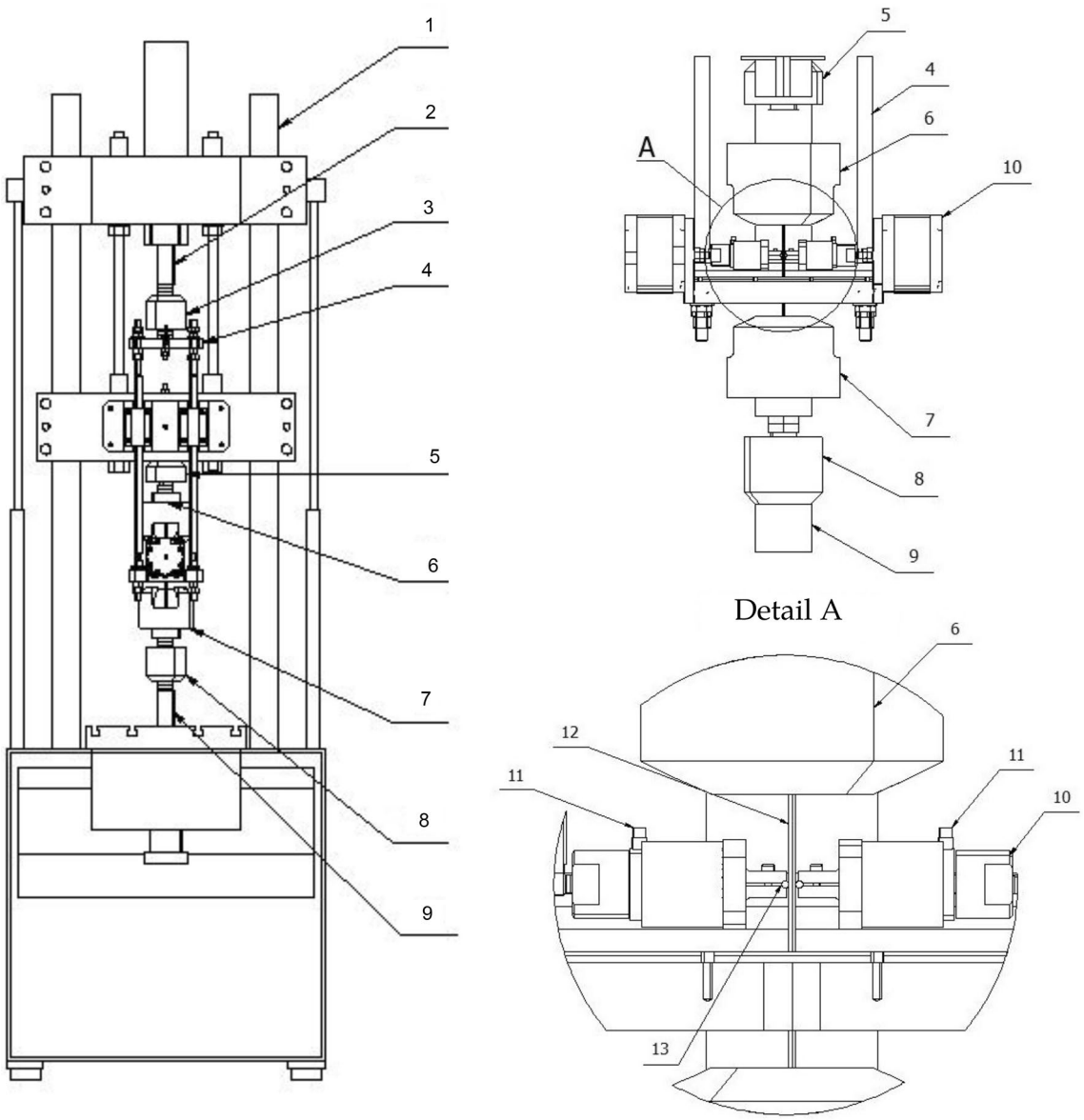

Fig. 2 Schematic view of the fretting rig, with detail viewing of the contact area

$$S_{\mathrm{m}} = \frac{S_{\max} + S_{\min}}{2}. \tag{3}$$

The stress-based fatigue life experimental tests of the 1350-H19 aluminum wires were performed with the help of a computer that controlled an 25 kN electrohydraulic fretting apparatus (Fig. 2). Figure 3 shows the schematic procedure adopted in order to impose fretting fatigue over the specimen. Two wires were used, Fig. 3a, where the pad was responsible to apply the normal load, P, over the specimen. Then, fretting fatigue conditions were caused by the cyclic micro-slip motion of the specimen due to an imposed bulk load, B. An additional tangential load, Q, could also be imposed at the far end of the pad. For this experiment, the specimen diameter was 3.139 mm with length of 220 mm. The lag angle between the axes of the pad and specimen was chosen to be 29°. With R set as 0.1, the P loads varied from 100 to 1600 N.

As a first analysis, no control was established over the Q load, being indirectly govern by B. Such approach ensured that both charges were in phase throughout the entire procedure. Finally, the B load was based on $S_{\max}$ values, which varied from 80 to 130 MPa, through the expression $S_{\max} = B/A$, where A is the cross-sectional area of the specimen. Figure 3b shows the side view of the experimental scheme, where it is possible to see the fixed pad, which applies a reactive load P over the specimen due to its non-moving condition.

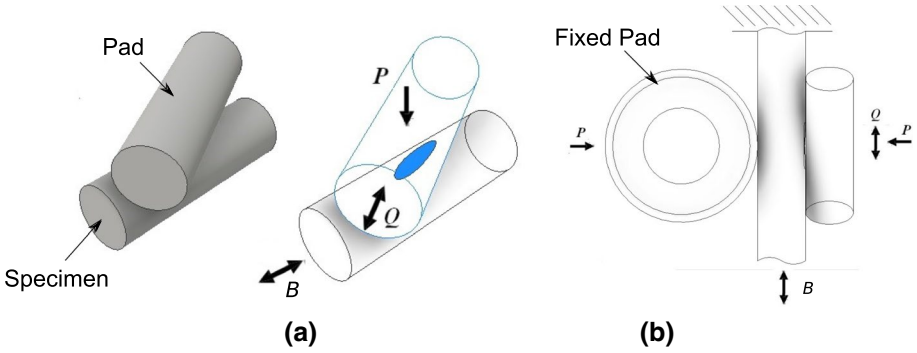

Fig. 3 Scheme of application of the loads in the experiment, **a** isometric view and **b** side view

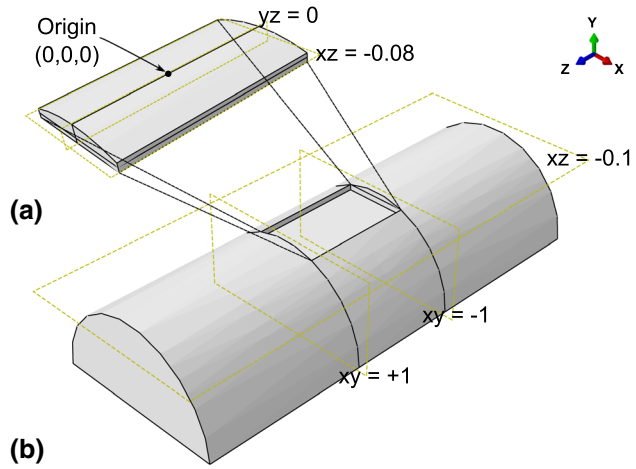

Fig. 4 **a** Contact region and **b** major structure

2.3 Numerical methodology

The simulation was performed using ABAQUS/CAE software, where the contact problem was modeled considering a semi-cylinder of 3.139 mm in diameter and 8 mm in length. Then, the body was partitioned at +1 mm and −1 mm with respect to the xy plane, and at −0.1 mm with respect to the xz plane, as shown in Fig. 4b. This procedure was carried out in order to cut and extrude the region that encompassed the contact zone. Surely after, a second part, with the exact measurements of the empty region, was made so that the mesh could be refined locally, Fig. 4a. This technique was inspired by the works of Cruzado et al.[11, 12] and was executed with the goal of reducing the computational costs associated with the contact simulation, since it makes possible to allocate, at these minor regions, small-sized contact elements. Also, in this part, two partitions at 0 and −0.08 mm with respect to the planes yz and xz, respectively, were made, which were necessary to ensure that the finite element mesh would be properly structured.

Afterward, both parts were coupled with a tie-constraint, generating one main structure. Finally, they were duplicated and assembled as the two bodies shown in Fig. 5, where the lower structure is the specimen and the upper one is the fretting pad. At this simulation, the lag angle between the axes of the pad and specimen was also chosen to be 29°.

According to ABAQUS User's manual[13], the software is able to distinguish two types of interactions, namely

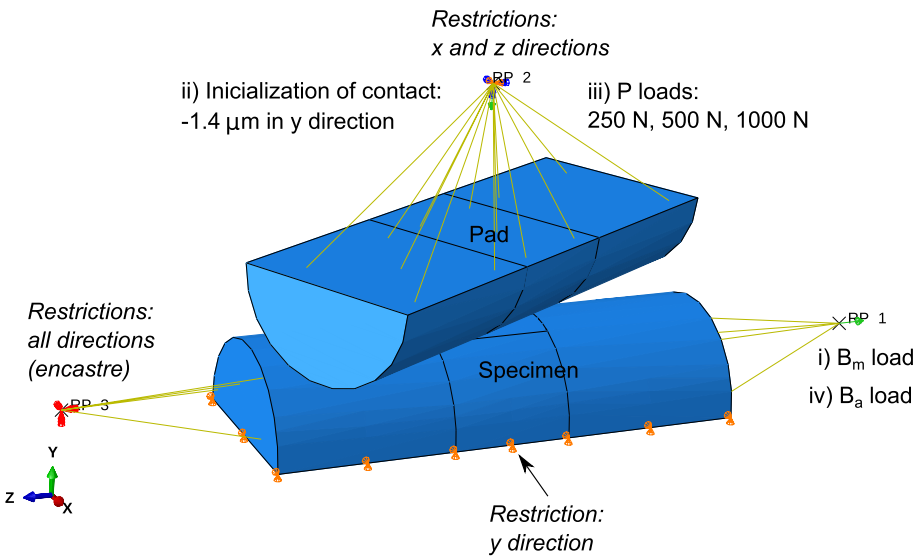

Fig. 5 Boundary conditions imposed in the simulation

equilibrium, in which the solution varies smoothly, or severe discontinuity (SDI), where abrupt changes in stiffness occur. The most common SDIs involves changes in the establishment of contact and friction regions. By default, ABAQUS will continue to iterate until the discontinuities are small enough to satisfy the equilibrium tolerances imposed by the software. However, the manually initialization of the contact, by the imposition of a very small displacement in one body toward the other (procedure known as indentation), offers an alternative approach in order to significantly reduce or completely eliminate severe discontinuities. This simple procedure stabilizes the contact simulation, decreases the number of iterations, and consequently, the computational costs involved. In addition, it reduces common problems such as the occurrence of chattering and pressure inaccuracies.

With this in mind, the process of applying the loads on the bodies was carried out in four general static steps, following the sequence: i) application of the average bulk load, B_m, ii) initialization of the contact by imposition of small displacements, iii) application of the P charge and iv) application of the alternating bulk load, B_a. All steps had 1 s period and standard automatic increments, except for the last one, referring to the application of the alternating bulk load, which had fixed increments of 0.025 s, generating 40 iterations. All boundary conditions (loads, displacements and restrictions) were applied to reference points (RPs) whose were attached, using kinematic coupling, to the free faces of the structures, as can be seen in Fig. 5 which also shows the efforts, enumerated according to the steps that they appear, as well as the restrictions (in italic letters). Here, it is important to highlight that the P loads were chosen as 250, 500 and 1000 N at the FEM analysis.

In order to define the interaction between the bodies, the surface-to-surface contact algorithm was used and the finite displacement formulation was implemented as a reinforcement method. Following Cruzado et al.[11], the contact surface of the pad was established as the slave and the surface of the specimen set as the master, in order to avoid convergence problems in small mesh sizes. The Lagrange multiplier algorithm was attributed to the surface contact behavior.

To compose the contact regions, continuous first-order, fully integrated, hexahedral elements (C3D8) were chosen, in order to avoid mesh locking and hourglassing. Then, continuous first-order tetrahedral elements (C3D4) were adopted to constitute the remaining zones of the solids in the simulation. A Python code was written containing all the simulation steps and procedures in order to be used directly at the ABAQUS/CAE command line interface, facilitating the reproducibility of the simulation. This code can be found in Appendix section of Pereira[14]. More information about the type and size of the elements, as well as the simulation outcomes, will be dealt with in Sect. 3.

Table 2 Fatigue models considered in this work[15, 16]

Model	Expression
Goodman	$S_{ar} = \frac{S_a}{1-(S_m/S_{ut})}$
Gerber	$S_{ar} = \frac{S_a}{1-(S_m/S_{ut})^2}$
Morrow	$S_{ar} = \frac{S_a}{1-(S_m/S_{fB})}$
Smith–Watson–Topper	$S_{ar} = \sqrt{S_a S_{max}}$
Walker[a]	$S_{ar} = S_{max}^{1-\gamma} S_a^{\gamma}$

[a] γ is an adjustable material parameter

2.4 Life estimate

A common approach to estimating the effect of mean stress on fatigue life is to express the S–N curve using Eq. 4:

$$S_{ar} = AN^b, \tag{4}$$

where S_{ar} is the equivalent fully reversed stress amplitude, A and b are fitting constants obtained under reverse loading conditions and N is the fatigue life. The equivalent fully reversed stress amplitude should be understood as a corrected stress that considers not only the presence of the mean stress, but also its effect on the behavior of the material. Although there are several models developed to explain the effect of average stress on fatigue behavior, only the most commonly used models[15, 16], presented in Table 2, are evaluated in this study.

The estimation of the parameters A and b of the S–N curve can be performed based on experimental data or from the approximation of the S–N diagram in the high cycle region[15, 17–20]. These authors report that assuming a situation in which the S–N curve passes through the points $(10^3, S_{10^3})$ and (N_{end}, S'_e), the parameters A and b can be obtained using the relations presented in Eqs. 5 and 6:

$$b = \frac{\log\left(\frac{S_{10^3}}{S'_e}\right)}{\log\left(\frac{10^3}{N_{end}}\right)}, \tag{5}$$

$$A = \frac{S_{10^3}}{10^{3b}}, \tag{6}$$

where N_{end} is the fatigue life corresponding to the endurance limit, S'_e. Lee et al.[15] comment that even though aluminum alloys do not have a true fatigue limit, a common practice is to take the fatigue strength at 5×10^8 cycles as the endurance limit (also referred as the pseudo fatigue limit value). The S_{10^3} value for the Al 1350-H19 is obtained from Kaufman[21] and is 210 MPa.

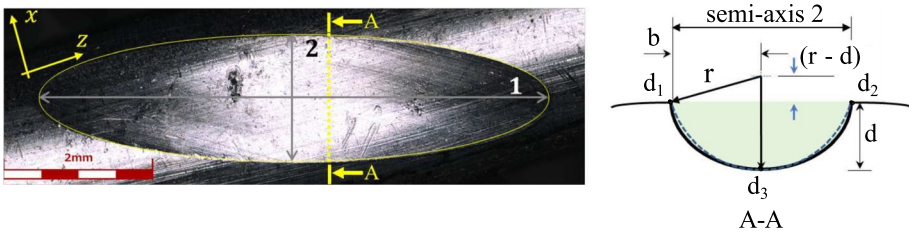

Fig. 6 **a** Top view marks generated by wire–wire contact and **b** schematic representation of the cross-sectional plane with the definition of the notch radius

In order to consider the service conditions of the wires in the conductive cables, Raoof[6], Knapp and Chiu[5] suggest that S'_e must be reduced, using Eq. 7, to account for the effects of surface finishing and the presence of stress raisers:

$$S_e = \frac{K_a S'_e}{K_f}, \tag{7}$$

where S_e is the reduced endurance limit, K_a is the surface finish factor and K_f is the fatigue notch factor. The K_a factor depends on the surface finish and tensile strength, and can be found from the literature[15, 17–20]. The surface finish is more critical for high-strength steel and at high-cycle fatigue lives, where crack initiation dominates the fatigue life[15]. The estimate of K_a was obtained from the available relations between this factor and the surface roughness, R_a[17]. In this sense, measurements of the surface roughness were made on the wire, which indicated a value of R_a equal to 0.1527 μ m. Thus, considering this roughness and the tensile strength limit of the aluminum wire, we adopted a value of 0.9 for the surface finishing factor. According to Bannantine et al.[17] the estimate of K_f can be made using the empirical formula proposed by Neuber, Eq. 8:

$$K_f = 1 + \frac{K_t - 1}{1 + \frac{\sqrt{\rho}}{\sqrt{r}}}. \tag{8}$$

In Eq. 8, K_t represents the elastic stress concentration factor, $\sqrt{\rho}$ is the Neuber's constant which, according to Kalombo et al.[22] for 1350-H19 aluminum alloys, is equal to 1.517 mm, and r is the notch root. Typically, under uniaxial load conditions, the calculation of K_t is performed considering the ratio between the maximum stress at the discontinuity, S_{max}, and nominal stress, S_{nom}. However, as the stress field generated in the notch is also caused by the stresses resulting from the wire-to-wire contact, Knapp and Chiu[5] proposed to redefine K_t calculation considering the relation presented in Eq. 9:

$$K_t = \frac{max(S_{mises})}{S_{nom}}, \tag{9}$$

where $max(S_{mises})$ correspond to the maximum Von Mises stress at the contact region. Because of the complex shape of the notch resulting from the contact process between the wires, it is more appropriate to estimate the K_t value and the notch root from the results obtained in the finite element modeling. Thus, $max(S_{mises})$ was obtained through the analysis of the Von Mises stress field and S_{nom} was estimated considering the maximum longitudinal stress, S_{zz}, acting on the wire contact region.

For the characterization, the notch radius was assumed that its value was associated with an arc of an imaginary circumference that intersected the points d_1 and d_2, which defined the smaller semi-axis of the projected ellipse on the xz plane (see Fig. 6a), and the point d_3, which defined the depth, d, of the contact mark (see Fig. 6b). From these considerations, the value of r was obtained from the calculation of the hypotenuse of the triangle rectangle with sides $(r - d)$ and b.

2.5 Life prediction: iterative procedure

Once the procedures for modeling the contact problem and the characterization of the S–N curve have been defined, it was possible to predict the fatigue life of the analyzed test specimens by means of an iterative approach. Hence, MATLAB® codes and ABAQUS/CAE procedures were developed based on the methodologies reported in Sects. 2.3 and 2.4. Figure 7 depicts a scheme of the strategy required to estimate the life of the wire under contact conditions. The first step is to define the conditions of the experimental test such as efforts, wire characteristics and stress ratio and obtain the experimental life. At this point, it is also possible to determine the alternating and mean stress components (respectively, S_a, and S_m) and calculate the equivalent fully reversed stress amplitude, S_{ar}, according to a specific model (equations presented in Table 2). The loading and boundary conditions are the inputs of the finite element model (Fig. 7

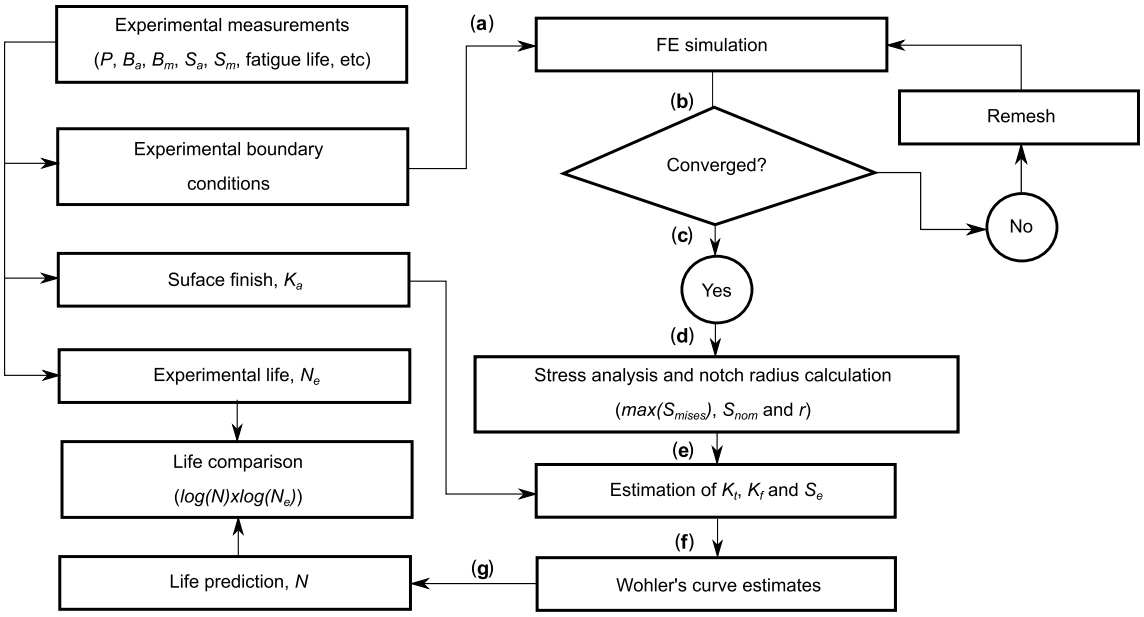

Fig. 7 Flow diagram summarizing the numerical procedures applied to predict the fatigue life

ramification (a)). In order to analyze the validity of the mesh, a convergence study needs to be made (Fig. 7 ramification (b) and (c)). In the refinement process, it used the technique of manual mesh adjustment at the contact region and the maximum Von Mises stress ($max(S_{mises})$) is adopted as a metric to evaluate the level of mesh convergence. Once the optimum mesh refinement condition is reached, the post-processing module is used to obtain the nominal stress, S_{nom}, and the notch radius, r, generated by the contact (Fig. 7 ramification (d)). With this information and knowing the material properties, it is possible to estimate the values of K_t (using Eq. 9) and K_f (using Eq. 8) and thus calculate the parameters of the Wohler's curve (using Eqs. 5 and 6) considering the reduced endurance limit, S_e. Finally, it is possible to predict the fatigue life by replacing S_{ar} in the Wohler's curves (Eq. 4) and then solve for N.

3 Results

3.1 Experimental results

The S–N curves, shown in Fig. 8a, present the results obtained by Díaz[23] for the fretting fatigue experimental tests carried out in 1350-H19 aluminum wires, considering normal loads of 250, 500 and 1000 N. To allow a more detailed analysis, the results that describe the material behavior, obtained with $R = 0.1$ under uniaxial conditions, are also given. All failures from 5×10^4 to 10^7 cycles were processed in the statistical analysis, assuming a log-linear distribution. The equations that represent the trend curves (solid lines) were estimated, considering the average geometric life (represented by the cross-shaped marks) observed for each stress level, by the application of the fitting technique. These expressions were introduced in a general form as Eq. 4 and are shown, for the respectively normal loads applied, in Eqs. 10, 11 and 12. Figure 8b shows the relations between the normal contact pressure, p, the projected indentation area, A, and several P loads observed during the study. The analysis of the correlations between p, A and P, as well as discussions about the experimental S–N curves, will be made in Sect. 4:

$$S_{\text{ar}} = 790.2N^{-0.147}, \tag{10}$$

$$S_{\text{ar}} = 1687.4N^{-0.207}, \tag{11}$$

$$S_{\text{ar}} = 576.7N^{-0.118}. \tag{12}$$

3.2 Numerical results

Regarding the size of the elements in the mesh, a convergence analysis was performed, where the maximum Von Mises stresses and contact pressures were observed for several different elements, as shown in Fig. 9. It was noticed that for sizes of 40 µm, 35 µm and 30 µm, the Von

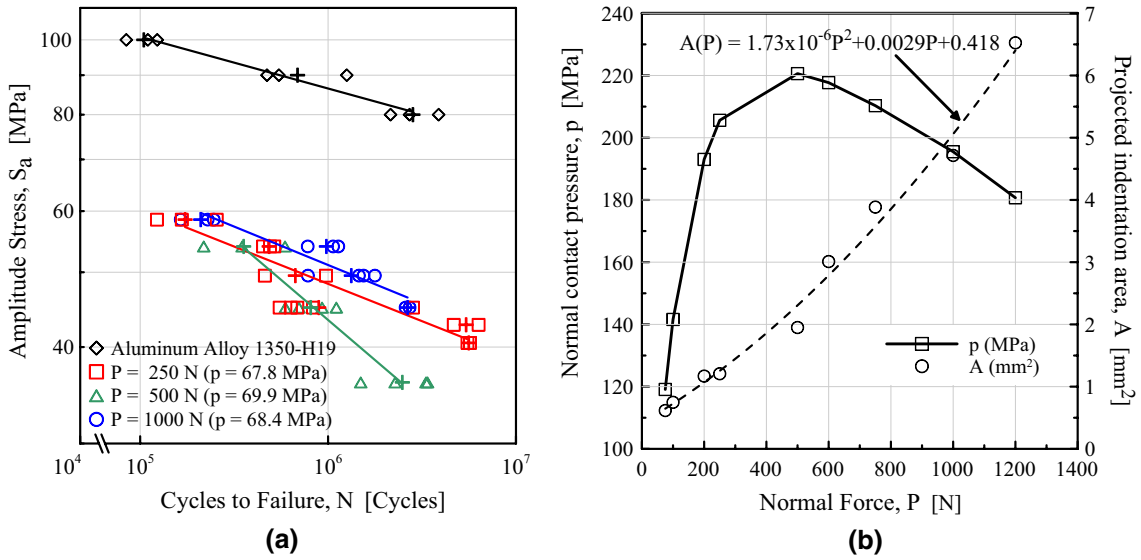

Fig. 8 **a** S–N curves for the 1350-H19 aluminum alloy under pure uniaxial and fretting conditions, **b** relations between contact pressure, indentation area and normal load

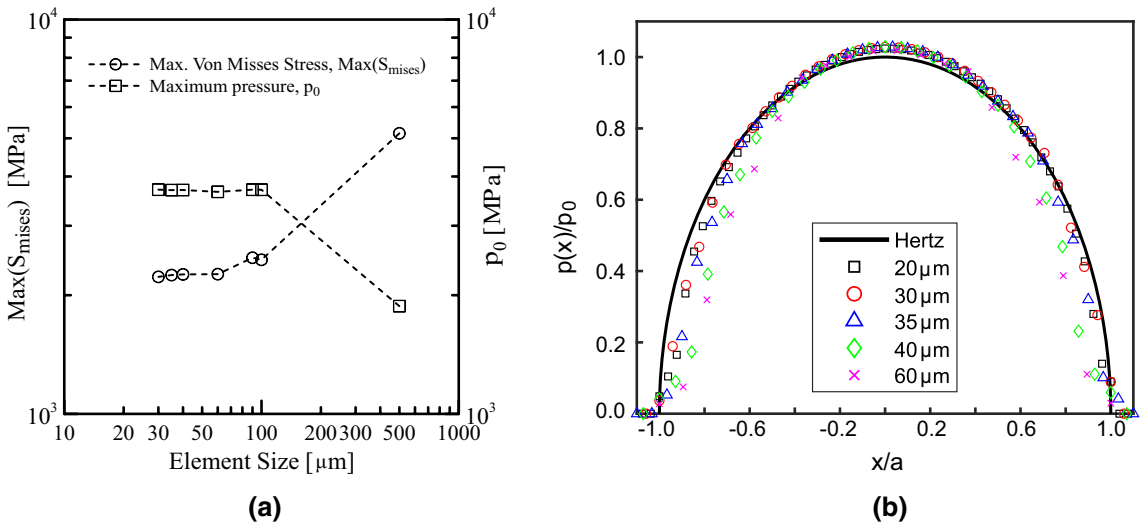

Fig. 9 **a** Von Misses stresses, **b** normalized contact pressures

Mises stresses stabilized in 2250 MPa and the maximum pressures around 3700 MPa, as can be seen in Fig. 9a. Now, looking at the contact pressures, Fig. 9b, it was found that the data for 35 μ m, 30 μ m and 20 μ m were close to the analytical Hertz model. It is also worth mentioning that, in this paper, a standard computer[1] was used in order to make the simulation accessible to most engineers,

Table 3 Analytical and numerical data comparison: $P = 250$ N

$P = 250$ N	Hertz	FEM	Error (%)
a (mm)	0.5891	0.5279	10.39
b (mm)	0.0916	0.1104	20.63
p_0 (MPa)	2213.4	2269.0	2.51

since the fatigue problem is of great importance to both the academic and industrial sectors. With this in mind, the computational costs were observed for 35 μm, 30 μm and 20 μm elements. For the first one, 2.5 hours were spent in

[1] Intel®Core™ i5-337U CPU @ 1.80GHz, 2 cores, 4 logic processors, 6.00 GB of RAM and NVIDIA GeForce GT 720M graphics card with integrated memory of 2 GB

Table 4 Analytical and numerical data comparison: $P = 500$ N

$P = 500$ N	Hertz	FEM	Error (%)
a (mm)	0.7422	0.6725	9.39
b (mm)	0.1154	0.1276	10.62
p_0 (MPa)	2788.6	2899.0	3.96

Table 5 Analytical and numerical data comparison: $P = 1000$ N

$P = 1000$ N	Hertz	FEM	Error (%)
a (mm)	0.9351	0.8510	8.99
b (mm)	0.1453	0.1577	8.48
p_0 (MPa)	3513.5	3694	5.14

order to full simulate the contact problem. For the second one, 6.5 hours were spent (2.6 times higher then the first). For the final one, 16 hours (6.4 times higher then the first) were consumed. All in all, due to its good correspondence to analytical data (Fig. 9b), stabilization of Von Mises stresses (Fig. 9a), relatively small errors (Tables 3, 4, 5) and lower computational costs, 35 µ m elements were chosen to be used at the contact zone.

As specified in Sect. 2.3, the contact zones were composed of C3D8 elements and the remaining regions of C3D4, in order to complete the solid. In these structures, elements of 35 µ m were implemented close to the contact zones and of 500 µ m at the far boundaries of the solids. This was made in order to prescribe a biased seed along the edges, completing the meshing process. This configuration gave rise to the data presented in Tables 3, 4 and 5, which brings a comparison between the ellipsoid contact marks, with major and minor semi-axis a and b, respectively, and the maximum pressure, p_0, obtained in the numerical (FEM) and analytical (Hertz) approaches, for P loads of 250 N, 500 N and 1000 N, respectively.

Additionally, the smaller the P load, applied to the wire-to-wire contact, is, the greater are the relative errors regarding a and b, which represents a decrease in the size of the contact mark, as well as a decrease in its resolution. This fact makes it difficult to know precisely were the mark starts and finishes, introducing errors in the measures of a and b. In addition, the central node of the contact mark changes, being also difficult to identify where the value of p_0 should be taken. All of these remarks indicate that a more refined mesh should be employed in cases where small values of P are considered. Despite that, it can be seen that the relative errors were, for the most part, lower than 10%. Figure 10a shows the assembly and mesh details of the FE model with expansion of its respective contact regions. In addition, Fig. 10b presents mesh details of the tie-constraint region of one of the bodies. Finally, Fig. 11 brings an example of the deformed mesh, with the contact mark highlighted by the pressure distribution along the body for $P = 1000$ N.

Tables 6, 7 and 8 show the maximum Von Mises stresses at the contact region, and the corresponding maximum and nominal stresses obtained, which are vital information in acquiring the fatigue life as informed in Sect. 2.4. From the FE simulation, the depths, d, of the contact marks were obtained for P loads of 250 N, 500 N and 1000 N, respectively. Then, the notch radius was calculated using the procedure stated also in Sect. 2.4, generating the results presented in Table 9, where the values of b were repeated for convenience.

Afterward, the models used to calculate the mean stress on fatigue behavior (see Table 2) were also considered in the numerical prediction of life. The outcome of this procedure was plotted against the experimental life, in a log–log scale, which can be seen in Fig. 12. It is important to note that, in all the graphs, two line deviations from the mean, of factor 3, were used in order to facilitate the comparison of the data. Finally, three values of P load were considered (250 N, 500 N and 1000 N), being also presented in Fig. 12.

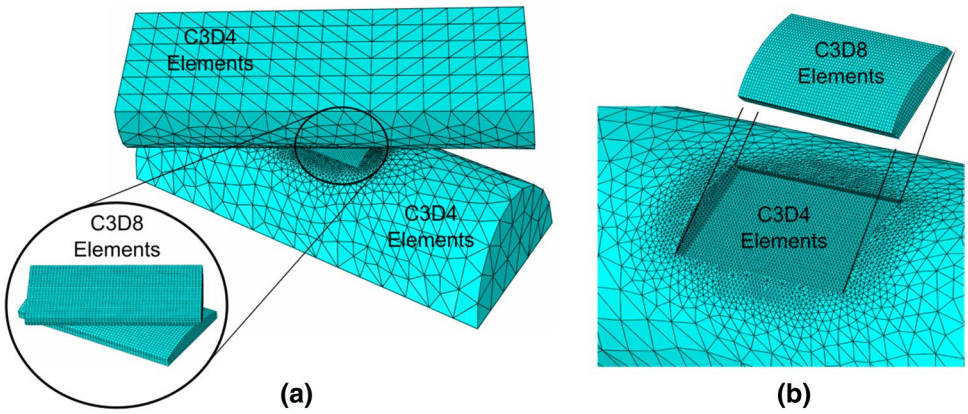

Fig. 10 **a** Complete assembly with expansion of the contact regions, **b** tie-constraint region

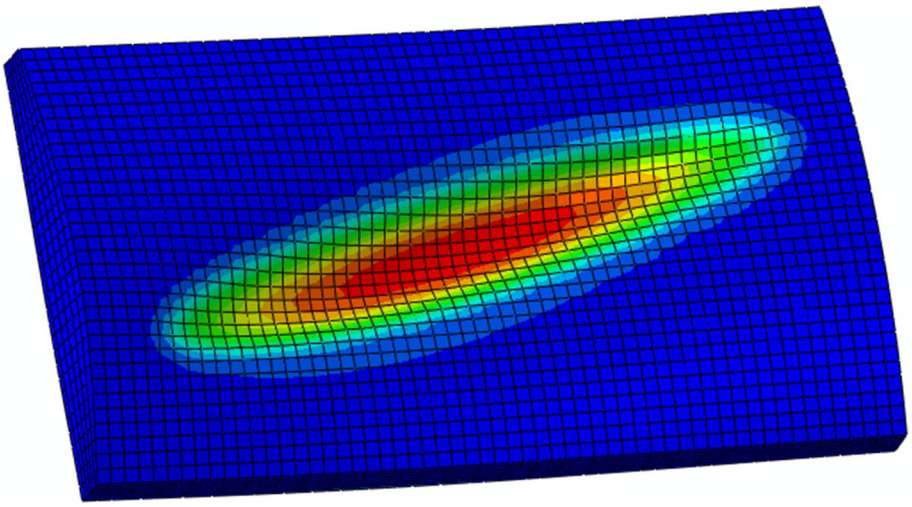

Fig. 11 Example of deformed mesh (uniform deformation scale factor of 10) with the contact mark highlighted by the pressure distribution along the body when $P = 1000\,\text{N}$

Table 6 Results obtained from the FEM: $P = 250\,\text{N}$

S_{max} (MPa)	Max (S_{mises}) (MPa)	S_{nom} (MPa)
80	1431	240.25
90	1443	248.11
100	1457	256.58
110	1550	265.06
120	1649	273.67
130	1693	289.93

Table 7 Results obtained from the FEM: $P = 500\,\text{N}$

S_{max} (MPa)	Max (S_{mises}) (MPa)	S_{nom} (MPa)
80	1752	301.09
90	1761	318.11
100	1770	302.61
110	1779	307.85
120	1790	313.77
130	1801	320.94

Table 8 Results obtained from the FEM: $P = 1000\,\text{N}$

S_{max} (MPa)	Max (S_{mises}) (MPa)	S_{nom} (MPa)
80	2227	321.63
90	2234	324.66
100	2241	320.73
110	2249	323.14
120	2257	317.56
130	2264	325.76

The detailed discussion about the influence of each mean stress model in the numerically predicted fatigue life, as well as the analysis of the experimental data, is addressed in the next section.

Table 9 Values of depth and notch radius

P (N)	b (mm)	d (mm)	r (mm)
250	0.1104	0.0097	0.6301
500	0.1276	0.0142	0.5817
1000	0.1577	0.0209	0.6058

4 Discussion

4.1 Experimental analysis

The analysis of the results presented in Fig. 8a clearly shows a tendency of the fretting fatigue curves to approach the material fatigue curve as the life decreases. Muñoz et al.[24], when studying the aluminum alloy 7075-T6 under fretting conditions, also observed such characteristics. According to these authors, for lives shorter than 10^6 cycles, a variation in the applied loads has less influence on life in fretting than on life in plain fatigue. This characteristic is also observed by Adriano et al.[25] and Martínez et al.[26] when studying the notch effect on the fatigue strength of alloy 6201; however, the authors did not make any observations regarding such behavior.

Considering that fretting fatigue damage will be assessed according to the notch analogue concept[27, 28], this behavior can be explained by the presence of high levels of deformation that occurs near the notches, in short and intermediate life regions, causing a blunting effect, which in turn leads to a local loss of sensitivity[15, 17]. In addition to the effect of increasing plasticity near the notches, it is also observed that although the normal loads are very different (250, 500 and 1000 N), the normal contact pressures (calculated by the ratio between the normal force and the projected area of the indentation) have the same order of magnitude.

Figure 8b shows the effect of the normal force, P, on the projected indentation area, A, and on the normal contact pressure, p. From the figure, it is possible to infer that the contact area tends to grow in a quadratic manner, mainly due to the intense permanent plastic deformation that occurs in the contact regions (see Fig. 6a). As the coefficient that multiplies the quadratic term is much smaller than the other two, the normal pressure tends to increase until reaching the maximum value of 220 MPa for a contact force of 500 N. Only then, the decrease starts.

4.2 Numerical analysis

In Goodman's model, Fig. 12a, it is possible to see that most part of the data is out of the range imposed by the deviation lines, except for P loads of 500 N which has only 9% of the data out of the lines. This configuration is also quite similar to the ones obtained when Morrow's and Smith-Watson-Topper's (SWT) models are considered, Fig. 12c, d, respectively. However, the tendency of the data is to be in the upper part of the mean line, which suggests that the numerically predicted results are, for the most part, conservative.

When looking at Fig. 12b, which shows Gerber's model, it can be noticed that almost all the data are inside the delimited zone, fact that indicates a good relation between the numerical and experimental data. On the other hand, for high fatigue lives, the results for 500 and 1000 N tend to get out of the deviation lines, with 14% and 9% of the data, respectively, out of the zone. In addition, the progression of these data seems to happen in opposite direction, which turns this model unpredictable to be used with other values of P.

In Walker's model, Fig. 12e, f, two values of γ were studied. First, γ was set to be 0.65, since the works of Dowling et al.[16] pointed that this value could be used with lower strength alloys like 6061-T6 and AlMg4.5Mn, for example. So, as the Al 1350-H19 is on the same range of ultimate tensile strength of these both alloys, the value of 0.65 was considered. However, it is observed that the data tend to the conservative side of the plot, especially for $P = 1000$ N, with 72% of the data above the upper deviation line. Then, γ was enhanced for 0.75, which shifted, in a factor of 1.5, all the results to the non-conservative side, fitting most of the data inside the range imposed by the deviation lines. Since the values of γ vary with the material and knowing that are no studies that provide the exact values of γ to be used with Al 1350-H19 in Walker's model, it is recommended that this model, combined with $\gamma = 0.75$, should be used with the methodology proposed in order to optimize the predictions.

5 Conclusions

The effect of contact between two 1350-H19 aluminum wires, on both experimental and numerical approaches, has been studied for three different values of normal load. The conclusions are as follows:

1. The experimental results show a tendency of the fretting fatigue curves to approach the material fatigue curve as the life decreases. For lives shorter than 10^6 cycles, a variation in the applied loads has less influence on life in fretting than on life in plain fatigue, which can be explained by the presence of high levels of deformation that occurs near the notches, in short and intermediate life regions. In addition, it is also observed that although the normal loads are very different, the normal contact pressures have the same order of magnitude.
2. Since the contact area tends to grow in a quadratic manner and its initial values are small, due to the small coefficient that multiplies the quadratic term, the normal pressure tends to increase until a maximum value of 220 MPa for a contact force of 500 N. Only then, the decrease starts.
3. The numerical results shows that, for the Goodman's model, as well as Morrow's and SWT's, part of the data is over the range lines imposed by a factor of 3, indicating that these models can be used to predict the fatigue lives of the Al 1350-H19 wires under fretting conditions, but the conservative results should be expected.
4. The Gerber's model presents a good prediction of the experimental results for the values of P considered in this work; however, due to its unpredictable behavior related to 500 and 1000 N data, it is indicated that this model cannot be used with general values of P.
5. Walker's model present, the most successful predictions, since most of the data fit inside the deviation lines. Moreover, in consideration that the adjustable material parameter has not yet been established for 1350-H19 aluminum alloy, it is recommended that this model, combined with $\gamma = 0.75$, should be used for the methodology proposed in order to optimize the occurrence of the predictions.

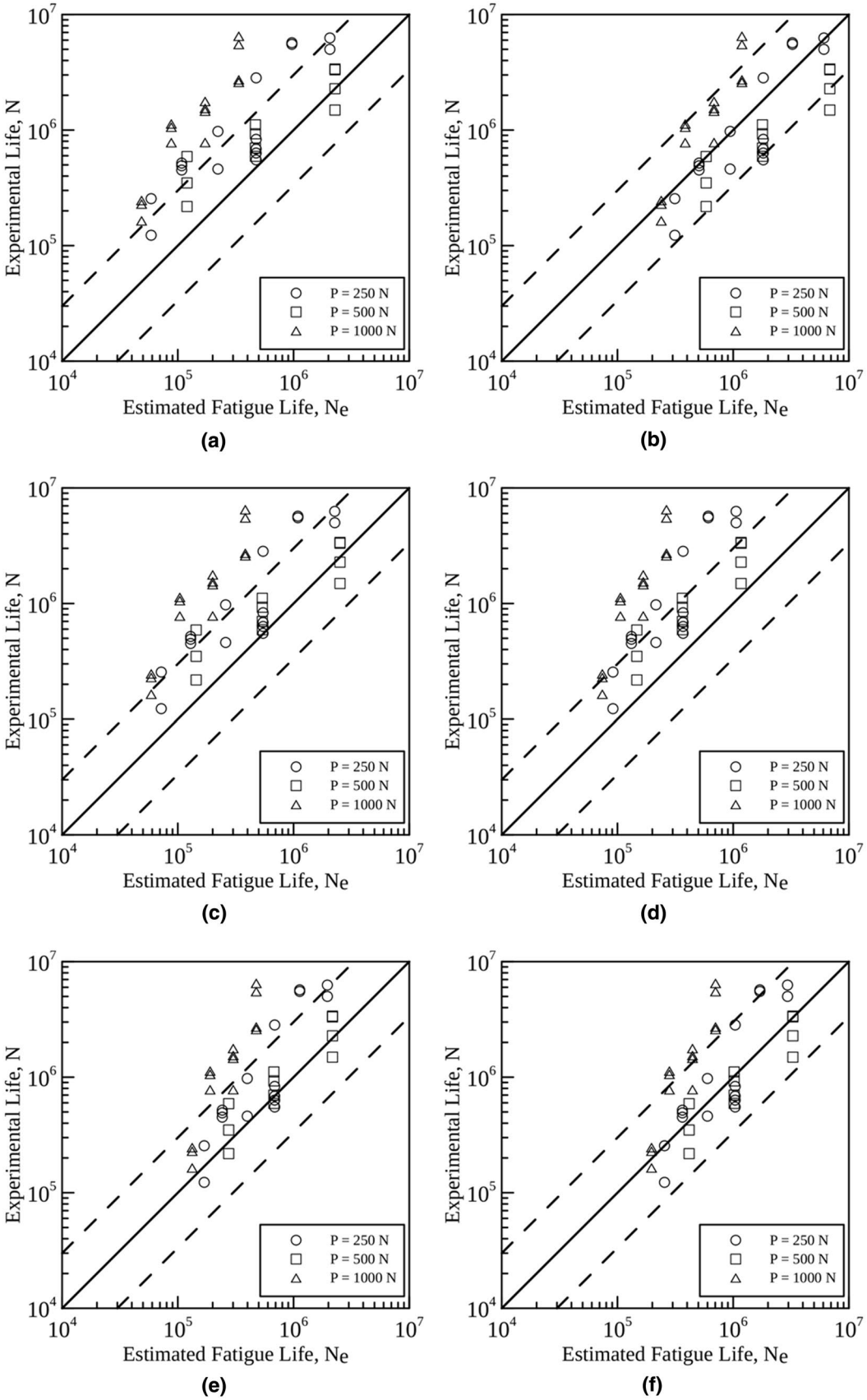
Experimental Life, N
Estimated Fatigue Life, Ne
P = 250 N
P = 500 N
P = 1000 N
(a)
(b)
(c)
(d)
(e)
(f)

◂**Fig. 12** Comparison of the experimentally and numerically predicted results considering each mean stress model, **a** Goodman, **b** Gerber, **c** Morrow, **d** SWT, **e** Walker with $\gamma = 0,65$ and **f** Walker with $\gamma = 0,75$

Compliance with ethical standards

Conflict of interest The authors declare that they have no conflict of interest.

Funding The authors would like to acknowledge the financial support of ENEL for the project entitled "Desenvolvimento de metodologia para redução de custos na estimativa de vida à fadiga de cabos condutores de energia." Additionally, the authors thank the financial support of Transmissoras Brasileiras de Energia (TBE) for the project entitled "Fadiga de Cabos de Alumínio Liga (CAL) 1120 e 6201: Estudo Comparativo, Efeito de Grampos AGS e de Emendas Pré-formadas". This project has been funded in the context of the Research and Development Program of the Brazilian National Agency of Electric Energy (ANEEL). Rodrigo L. Pereira and José I. M. Díaz were financed by the Coordenação de Aperfeiçoamento de Pessoal do Nível Superior—Brasil (CAPES)—Finance Code 001. Cosme R. M. da Silva, José A. Araújo and Jorge L. A. Ferreira are also grateful for the support provided by the Conselho Nacional de Desenvolvimento Científico e Tecnológico (CNPq)—contracts 306468/2018-2, 305302/2017-5 and 301366/2018-7.

References

1. Hills DA, Nowell D (1994) Mechanics of fretting fatigue. Kluwer, Waterloo
2. Araújo JA, Susmel L, Taylor D, Ferro JCT, Ferreira JLA (2008) On the prediction of high-cycle fretting fatigue strength: theory of critical distances vs. hot-spot approach. Eng Fract Mech 75:1763–1778
3. Zhou ZR, Cardou A, Fiset M, Goudreau S (1994) Fretting fatigue in electrical transmission lines. Wear 173:179–188
4. Zhou ZR, Goudreau S, Fiset M, Cardou A (1995) Single wire fretting fatigue tests for electrical conductor bending fatigue evaluation. Wear 181:537–543
5. Knapp RH, Chiu EYC (1988) Tension fatigue model for helically armored cables. J Energ Resour ASME 110:12–18
6. Raoof M (1990) Axial fatigue of multilayered strands. J Eng Mech 116:2083–2099
7. Hobbs RE, Raoof M (1996) Behaviour of cables under dynamic or repeated loading. J Constr Steel Res 39:31–50
8. Thomas HR, Hoersh VA (1930) Stresses due to pressure of one elastic solid upon another. Bulletin no. 212, Engrg. Exp. Sta., University of Illinois, Urbana, IL, USA
9. Wokem C (2015) Fatigue prediction for strands and wire ropes in tension and bent over sheave wheel. PhD Thesis, University of Alberta, Department of Civil and Environmental Engineering, Alberta, Canada
10. Wokem C, Joseph T, Curley M (2018) Fatigue life prediction for cables in cyclic tension. J Strain Anal Eng 53:141–155
11. Cruzado A, Urchegui MA, Gómez X (2012) Finite element modeling and experimental validation of fretting wear scars in thin steel wires. Wear 289:26–38
12. Cruzado A, Urchegui MA, Gómez X (2014) Finite element modeling of fretting wear scars in the thin steel wires: application in crossed cylinder arrangements. Wear 318:98–105
13. Systèmes Dassault (2012) Abaqus analysis user's manual, vol II. Simulia Corp, Rhode Island
14. Pereira RL (2018) Predição da Vida em Fadiga sob Condições de Fretting de um Fio de Alumínio 1350-H19 Utilizando o Método dos Elementos Finitos. Master's Thesis, University of Brasília, Department of Mechanical Engineering, DF, Brazil
15. Lee Y, Pan J, Hathaway R, Barkey M (2005) Fatigue testing and analysis: theory and practice. Elsevier, Oxford
16. Dowling NE, Calhoun CA, Arcari A (2009) Mean stress effects in stress-life fatigue and the walker equation. Fatigue Fract Eng Mater 32:163–179
17. Bannantine JA, Comer JJ, Handrock JL (1990) Fundamentals of metal fatigue analysis. Prentice Hall, Upper Saddle River
18. Budynas RG, Nisbett JK (2011) Shigley's mechanical engineering design. McGraw-Hill, New York
19. Dowling NE (2013) Mechanical behavior of materials: engineering methods for deformation, fracture, and fatigue. Pearson, Essex
20. Juvinall RC, Marshek KM (2011) Fundamentals of machine components design. Wiley, New York
21. Kaufman JG (2008) Properties of aluminum alloys: fatigue data and the effects of temperature, product form, and processing. ASM International, Ohio
22. Kalombo RB, Martínez JMG, Ferreira JLA, da Silva CRM, Araújo JA (2015) Comparative fatigue resistance of overhead conductors made of aluminum and aluminum alloy: tests and analysis. Proc Eng 133:223–232
23. Díaz JIM (2018) Avaliação do Efeito do Fretting Sobre o Comportamento à Fadiga de Fios Fabricados com Liga de Alumínio Al 1350-H19. Master's Thesis, University of Brasília, Department of Mechanical Engineering, DF, Brazil
24. Muñoz S, Navarro C, Domínguez J (2007) Application of fracture mechanics to estimate fretting fatigue endurance curves. Eng Fract Mech 74:2168–2186
25. Adriano VSR, Martínez JMG, Ferreira JLA, Araújo JA, da Silva CRM (2018) The influence of the fatigue process zone size on fatigue life estimations performed on aluminum wires containing geometric discontinuities using the theory of critical distances. Theor Appl Fract Mech 97:265–278
26. Martínez JMG, Adriano VSR, Araújo JA, Ferreira JLA, da Silva CRM (2019) Geometrical size effect in the fatigue life predictions of aluminum wires with micro holes using methods of the critical distance. Eng Fract Mech 209:147–161
27. Teuchou Kouanga CV, Jones JD, Revill I, Wormald A, Nowell D, DwyerJoyce RS, Araújo JA, Susmel L (2018) Finite lifetime estimation of mechanical assemblies subjected to fretting fatigue loading. In: Abdel Wahab M (eds) Proceedings of the 7th international conference on fracture fatigue and wear: FFW 2018
28. Araújo JA, Susmel L, Pires MST, Castro FC (2017) A multiaxial stress-based critical distance methodology to estimate fretting fatigue life. Tribol Int 108:2–6